COMMUNICATIONS CHEMISTRY

ARTICLE

DOI: 10.1038/s42004-018-0010-6 OPEN

Direct synthesis and in situ characterization of monolayer parallelogrammic rhenium diselenide on gold foil

Shaolong Jiang[1,2], Min Hong[1,2], Wei Wei[3], Liyun Zhao[1], Na Zhang[2], Zhepeng Zhang[1,2], Pengfei Yang[1,2], Nan Gao[4], Xiebo Zhou[1,2], Chunyu Xie[1,2], Jianping Shi[1,2], Yahuan Huan[1,2], Lianming Tong[2], Jijun Zhao[4], Qing Zhang[1], Qiang Fu[3] & Yanfeng Zhang[1,2]

Rhenium diselenide ($ReSe_2$) has recently garnered great research interest due to its distorted 1T structure, anisotropic physical properties, and applications in polarization-sensitive photodetectors. However, $ReSe_2$ synthesized by chemical vapor deposition (CVD) is usually a multilayer/polycrystalline material containing numerous grain boundaries, thereby hindering its further applications. Here we describe the direct CVD growth of high-quality monolayer $ReSe_2$ single crystals with a parallelogram shape arising from its anisotropic structure on a gold foil substrate. In particular, we use low-energy electron microscopy/diffraction combined with scanning tunneling microscopy/spectroscopy to determine the atomic-scale structure, domain orientation/boundaries, and band features of monolayer $ReSe_2$ flakes grown directly on gold foils. This work may open new opportunities for the direct synthesis and in situ characterization of CVD-grown monolayer $ReSe_2$.

[1] Department of Materials Science and Engineering, College of Engineering, Peking University, Beijing 100871, China. [2] Center for Nanochemistry (CNC), Beijing National Laboratory for Molecular Sciences, College of Chemistry and Molecular Engineering, Peking University, Beijing 100871, China. [3] State Key Laboratory of Catalysis, Collaborative Innovation Center of Chemistry for Energy Materials (iChEM), Dalian Institute of Chemical Physics, Chinese Academy of Science, Dalian 116023, China. [4] Key Laboratory of Materials Modification by Laser, Ion and Electron Beams, Dalian University of Technology, Ministry of Education, Dalian 116024, China. These authors contributed equally to this work: Shaolong Jiang, Min Hong. Correspondence and requests for materials should be addressed to Q.F. (email: qfu@dicp.ac.cn) or to Y.Z. (email: yanfengzhang@pku.edu.cn)

Inspired by graphene research[1–3], researchers in science and technology have recently shown increasing interest in two-dimensional (2D) monolayer transition metal dichalcogenides (TMDs, e.g., MoS_2 and WS_2) due to their rich physical, chemical, and electronic properties associated with the dimensionality effect[4–10]. Rhenium dichalcogenides (ReX_2, X = S or Se) are an emerging class of TMDs which, unlike high-symmetry hexagonal TMDs, crystallize in a distorted $CdCl_2$ structure with a triclinic symmetry due to charge decoupling from an additional valence electron in each Re atom[11, 12]. The distortion of the crystal structure affords weak interlayer coupling[13–15], making bulk ReX_2 behave as electronically and vibrationally decoupled monolayers. Accordingly, the transition from indirect to direct band gap is not observed in three-atom-thick ReX_2, which is in sharp contrast with hexagonal semiconducting TMDs. More intriguingly, ReX_2 exhibits a low-symmetry crystal lattice owing to its distorted structure, and the resulting anisotropic electrical and optical properties[16–20] enable applications in polarization-sensitive photodetectors and integrated polarization controllers (such as wave plates)[21–23].

Driven by such intriguing properties, researchers have devoted substantial efforts to synthesize monolayer or few-layer $ReSe_2$ through various routes, including mechanical exfoliation[12, 19, 20] and chemical vapor deposition (CVD)[22, 24, 25]. Notably, adhesive tape-based mechanical exfoliation yielded high-quality $ReSe_2$ flakes from bulk crystals but suffered from unsatisfactory control of the domain size and thickness[12, 19, 20]. The facile CVD technique was then utilized to fabricate $ReSe_2$ flakes on diverse dielectric substrates, rendering $ReSe_2$ flakes with obvious thickness variations and polycrystalline domains[22, 24, 25]. Additionally, the current characterization routes for recognizing the grain boundaries (GBs) of polycrystalline $ReSe_2$ are still limited to Raman spectroscopy or ex situ transmission electron microscopy (TEM)[24, 26]. Additional facile, high-throughput, and in situ identification routes that can evaluate materials from the atomic scale to the domain scale and can effectively achieve characterization of their morphological and electronic properties are still missing despite their importance for guiding the synthesis of samples with controlled orientations and properties.

A system for $ReSe_2$ growth on a conductive substrate, which is distinct from its growth on insulating substrates, should hold fundamental promise considering its compatibility with powerful characterization techniques such as low-energy electron microscopy/diffraction (LEEM/LEED) and scanning tunneling microscopy/spectroscopy (STM/STS). Multi-scale structural details, as well as electronic properties, can be determined to provide insights into related systems[27, 28]. Coincidentally, a surface self-limited growth mechanism has recently been proposed by our group and other researchers for achieving high-quality monolayer MX_2 (M: Mo, W; X: S, Se) on a unique Au foil substrate due to the low solubility of Mo, W, S and Se in Au[29–32]. The extremely low solubility (nearly 0.1 at.% at 1000 °C) of Re in Au[33] may therefore be exploited to develop a new $ReSe_2$/Au growth system.

Herein, we demonstrate direct synthesis of high-quality monolayer $ReSe_2$ single crystals on a gold foil substrate via an ambient-pressure CVD (APCVD) route based on a surface self-limited growth mechanism. Using Raman spectroscopy, TEM, and LEEM/LEED, we correlate the lattice orientation and crystallinity with the specific domain shape, thereby establishing a common rule for identifying the single-crystal domain of the structurally anisotropic $ReSe_2$ (e.g., to determine whether the parallelogram-shaped $ReSe_2$ domain is monocrystalline). By virtue of high-resolution STM/STS, we also uncover the atomic-scale structures, defects (mainly GBs), and energy band feature of our high-quality monolayer $ReSe_2$ on Au foils, none of which have been addressed to date, especially regarding CVD-grown $ReSe_2$ samples.

Results

APCVD synthesis and TEM characterization of monolayer $ReSe_2$. The growth process of $ReSe_2$ on the Au foil substrate is schematically displayed in Fig. 1a. Details on the growth methodology and experimental setup are provided in the Methods section and Supplementary Fig. 1, respectively. In brief, the ReO_3 powder precursor (downstream) partially decomposes into highly volatile Re_2O_7 via a disproportionation reaction, and this product is subsequently transported by the Ar and H_2 carrier gases and reacted with the Se precursor (upstream) to form $ReSe_2$ flakes/films on the Au substrate. In this process, the Au surface is very inert towards the Se precursor, and surface reactions other than that involved in the $ReSe_2$ synthesis should not occur.

X-ray photoelectron spectroscopy (XPS) was first employed to identify the formation of $ReSe_2$ on Au foils. Five elements were observed in the full-range XPS spectrum (Supplementary Fig. 2). As also representatively shown in Fig. 1b, the Se 3*d* spectrum consists of two peaks located at binding energies of 55.8 and 54.9 eV, which correspond to Se $3d_{3/2}$ and Se $3d_{5/2}$, respectively, and the Re 4*f* spectrum possesses two peaks located at 44.2 and 41.8 eV, which are consistent with Re $4f_{5/2}$ and Re $4f_{7/2}$, respectively. The peak at 57.7 eV is attributed to Au $5p_{3/2}$, which arises from the Au substrate. The shifts to lower binding energies for Se 3*d* and Re 4*f* relative to those previously reported (Se $3d_{3/2}$: 56.0 eV; Se $3d_{5/2}$: 55.1 eV; Re $4f_{5/2}$: 44.4 eV; Re $4f_{7/2}$: 42.0 eV) for monolayer $ReSe_2$ on SiO_2/Si[25] should result from the relatively strong electronic interaction of $ReSe_2$/Au. In short, the XPS data provide tentative evidence for the evolution of $ReSe_2$ on Au foils.

Scanning electron microscopy (SEM) images of the as-grown $ReSe_2$ flakes on Au foils were then obtained, as shown in Fig. 1c,d and Supplementary Fig. 3. Uniform parallelogrammic shapes with a specific angle of ~119° are noticeable between the long and short edges, which is almost equal to the angle (118.91°) between the *a*-axis and *b*-axis of the $ReSe_2$ crystal[22]. Moreover, the well-defined parallelogrammic shape can be preserved under different growth time (from 15 to 30 min), but with the long-edge lengths varying from ~2 to ~20 μm, as shown in Fig. 1c,d. In this regard, relatively good crystallinity and unique lattice orientation can be expected for such parallelogram-shaped flakes. More intriguingly, the ratio of the long/short edge length for the parallelogram-shaped $ReSe_2$ can reach 5.5:1 (Fig. 1d), strongly suggesting anisotropic growth along different lattice orientations. Most of the $ReSe_2$ domains displayed in Fig. 1c appear to have similar edge directions to each other, which is probably mediated by the steps of the crystalline facets of Au (mainly Au(100)[28]), i.e., the $ReSe_2$ domains are aligned with one of their edges along the steps of the Au facets. More generally, the $ReSe_2$ domains grown on a single Au domain/facet possess different orientations, as shown by the SEM image and its statistical analysis in Supplementary Fig. 3a, b. The lack of strict correlation between the crystal orientation of the $ReSe_2$ domain and the underlying Au implies that there is no definite epitaxial relationship between the two. This phenomenon was also observed for monolayer MoS_2 synthesized on Au foils[29].

The transfer of APCVD-synthesized $ReSe_2$ from Au foils to SiO_2/Si substrates or TEM grids is highly important for further flake thickness and crystal structure characterization. In this study, a previously developed electrochemical bubbling method[30] was exploited to transfer the as-grown sample because of its environmental friendliness. Atomic force microscope (AFM) images of $ReSe_2$ flakes transferred onto SiO_2/Si are presented in Fig. 1e and Supplementary Fig. 4, showing good maintenance of the initial parallelogrammic shape. The apparent flake height was measured as ~0.9 nm (inset of Fig. 1e), highly indicative of its monolayer nature according to previously published data[12]. More AFM data are supplied in Supplementary Fig. 4.

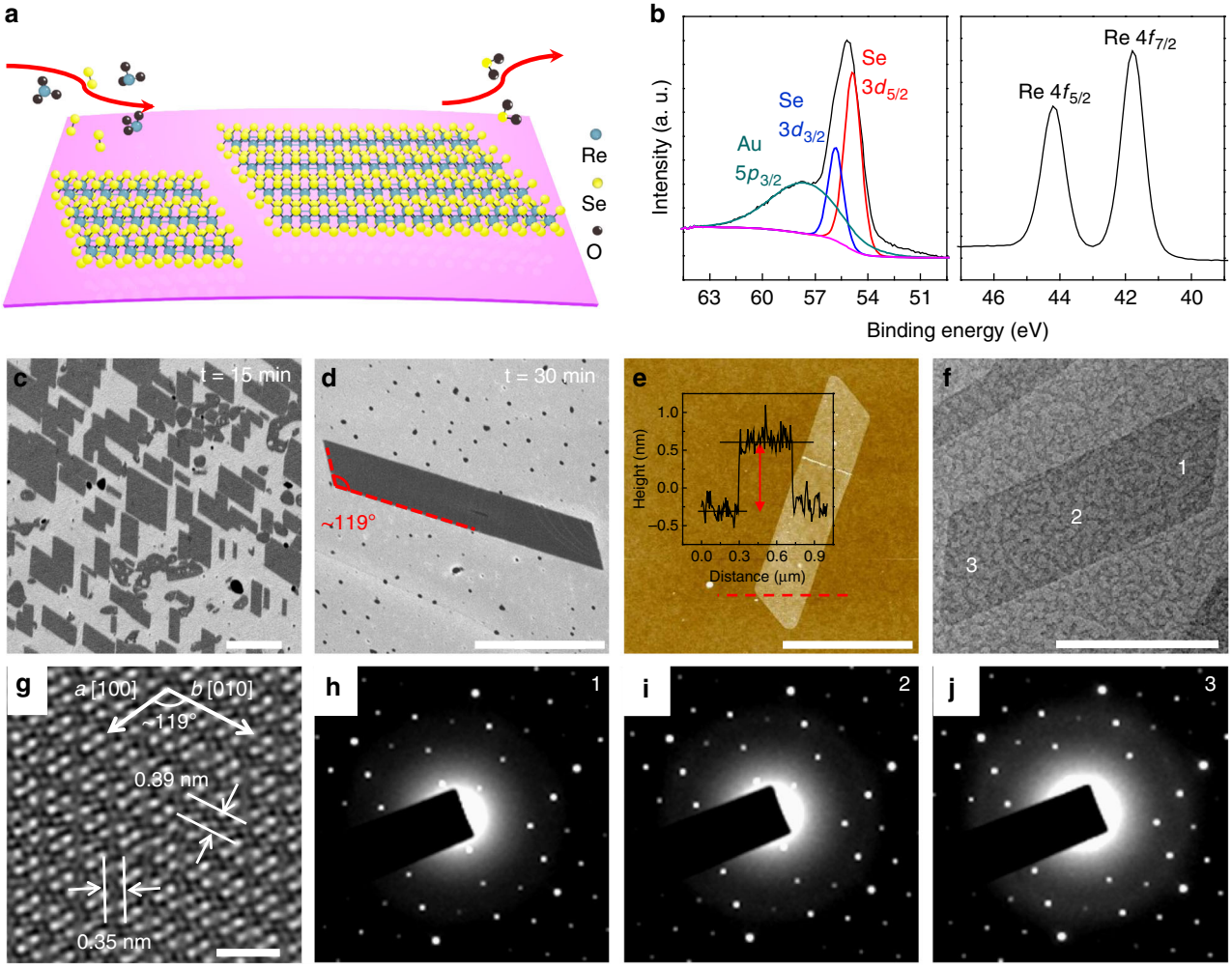

Fig. 1 APCVD synthesis and characterization of monolayer $ReSe_2$ flakes. **a** Schematic diagram of the surface-mediated growth of $ReSe_2$ on the Au foil. **b** XPS spectra showing Se 3*d* and Re 4*f* peaks in an as-grown sample, confirming the formation of $ReSe_2$. **c**, **d** Typical SEM images of the parallelogram-shaped $ReSe_2$ achieved at different growth times: **c** 15 min and **d** 30 min (under 50 sccm Ar and 10 sccm H_2). **e** Representative AFM image of a $ReSe_2$ flake transferred onto SiO_2/Si showing a representative monolayer thickness of ~0.9 nm (red arrow). **f** TEM image of a parallelogram-shaped $ReSe_2$ flake transferred onto a TEM grid. **g** Characteristic STEM image presenting the perfect atomic lattice. **h–j** Three typical SAED patterns collected from the areas labeled 1–3 in **f** revealing nearly identical lattice orientations over the whole flake. Scale bars, 2 μm in **c**, 5 μm in **d**, 1 μm in **e**, 500 nm in **f** and 1 nm in **g**

To clarify the detailed structure, TEM and spherical-aberration-corrected scanning transmission electron microscopy (STEM) analyses were also performed for a parallelogram-shaped $ReSe_2$ flake transferred onto a copper TEM grid, as shown in Fig. 1f. A representative TEM image of the folded $ReSe_2$ flake edge revealed a width of ~0.69 nm for the bright line, further indicating its monolayer feature (Supplementary Fig. 5). Specifically, monolayer $ReSe_2$ crystalizes in a stably distorted 1T structure with a diamond-shape Re_4 chain along the *b*[010] direction, as shown from the high-resolution STEM image in Fig. 1g. The angle measured between the *b*[010] and *a*[100] axes was ~119°, and the lattice spacing between the two vicinal diamond-shaped chains in the respective directions were ~0.39 and ~0.35 nm, agreeing well with those of the exfoliated sample[26]. Selected-area electron diffraction (SAED) patterns of three typical locations of a transferred flake (marked 1 to 3 in Fig. 1f) were also collected to show the same crystallographic orientation (Fig. 1h–j).

The above characterization results indicate that the monolayer $ReSe_2$ flakes universally observed with an ideal parallelogrammic shape should be single-crystalline domains. The monolayer thickness can be maintained until the complete coverage of the substrate by the $ReSe_2$ film by extending the growth time to 60 min (Supplementary Fig. 3e). Similar to the mechanisms of monolayer graphene growth on Cu foils[34] and of monolayer MoS_2 or WS_2 growth on Au foils[29–31], a self-limited catalytic growth mechanism is thus proposed for $ReSe_2$/Au foils for the following reasons: (1) the Au substrate is more catalytically active for the synthesis of high-quality $ReSe_2$ than the inert insulating substrates, and (2) the solubility of Re in Au is extremely low (nearly 0.1 at.% at 1000 °C), which allows the surface-catalyzed growth of $ReSe_2$ with a monolayer thickness.

Optical properties of single-crystal monolayer $ReSe_2$ domains. Figure 2a shows representative Raman spectra obtained using a 532 nm laser for as-grown $ReSe_2$ flakes on Au foils and transferred on SiO_2/Si. More than 10 distinctive Raman peaks are visible in the range of 100–300 cm^{-1} owing to the low crystal symmetry of $ReSe_2$. For the as-grown $ReSe_2$ flake on Au foils, two obvious Raman peaks at ~122 and ~158 cm^{-1} were detected and assigned to E_g-like and A_g-like vibrational modes, respectively. Notably, the two peaks were redshifted by ~2 cm^{-1} compared

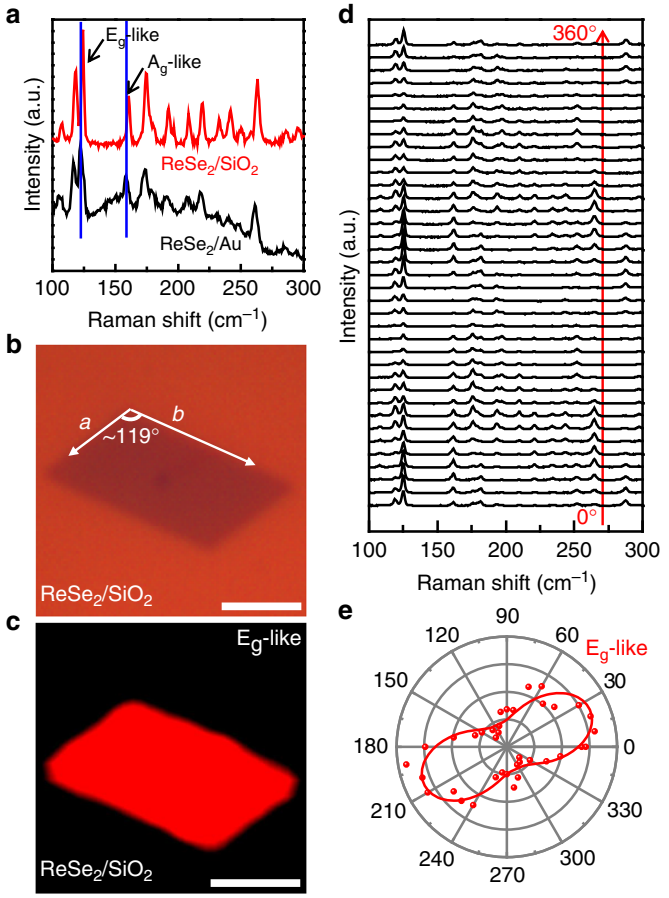

Fig. 2 Optical properties of parallelogram-shaped monolayer $ReSe_2$ single crystals transferred onto a SiO_2/Si substrate. **a** Comparison of the Raman spectra of as-grown $ReSe_2$ on Au foils and transferred on SiO_2/Si. **b**, **c** Optical image and corresponding Raman intensity mapping image of the E_g-like peak of a typical $ReSe_2$ polygon. **d** Angle-dependent polarized Raman spectra of the $ReSe_2$ flake transferred onto SiO_2/Si under the parallel polarization configuration with a 514 nm laser for excitation. **e** Polar plot of the Raman E_g-like peak intensities with different sample rotation angles. Scale bars, 2 μm in **b**, **c**

with those (E_g-like and A_g-like vibrational modes at ~124 and ~160 cm^{-1}, respectively) observed after transfer onto SiO_2/Si and with previous results for CVD-grown $ReSe_2$ on SiO_2/Si[22]. This redshift is attributed to an enhanced adlayer-substrate interaction of $ReSe_2$/Au according to previous work for MoS_2/Au[28, 35]. To confirm the crystal quality of the monolayer $ReSe_2$ flakes, Raman spectroscopy/mapping measurements were also carried out with a laser wavelength of 532 nm. A representative optical image and corresponding Raman intensity mapping image (the E_g-like vibrational mode) for the parallelogram-shaped $ReSe_2$ transferred onto SiO_2/Si are presented in Fig. 2b,c. Importantly, the Raman intensity is rather uniform across the whole domain, strongly indicating its rather high thickness homogeneity.

Figure 2d shows a series of polarized Raman spectra of the parallelogram-shaped $ReSe_2$ flake transferred onto SiO_2/Si that were collected at different sample rotation angles (from 0° to 360° with an interval of 10°) under the parallel polarization configuration with a 514 nm laser. Notably, the peak intensities of all the Raman modes are strictly dependent on the sample rotation angle, as clearly shown in the polar plot of the E_g-like mode intensity (Fig. 2e). These Raman data are well consistent with previous reports[22, 24], thereby confirming the anisotropic nature of the single-crystal domain and denoting the specific edge orientations in the crystallization process, i.e., the alignments of the *a*-axis or *b*-axis along the short or long edges of the parallelogrammic $ReSe_2$ domain[22]. Briefly, angle-resolved polarized Raman spectroscopy is suitable for identifying the optical in-plane anisotropy, as well as the crystalline orientation of our transferred monolayer single-crystal $ReSe_2$.

LEEM and LEED characterization of monolayer $ReSe_2$. Considering the in situ imaging ability and the complementary diffraction function of LEEM[27, 36–38] and the conductivity of $ReSe_2$/Au foils, bright-field LEEM (BF-LEEM) was then utilized to image the crystalline structure of the $ReSe_2$ parallelogram, as shown in Fig. 3a. Corresponding micro-region LEED (μ-LEED) patterns were also collected from representative regions marked 1–3 in Fig. 3a (selected regions of 2 μm in diameter). Nearly identical lattice orientations can be observed in Fig. 3b, accordingly indicating the single-crystal feature of the monolayer parallelogram-shaped $ReSe_2$ domains, in good agreement with the TEM and SAED results in Fig. 1. Additional LEEM/LEED characterization of the crystalline structure of the $ReSe_2$ parallelogram is described in Supplementary Fig. 6.

For more evidence, representative BF-LEEM and corresponding LEED characterization of three discrete $ReSe_2$ parallelograms was also performed (Supplementary Fig. 7a). Interestingly, the dark-field LEEM (DF-LEEM) image shown in Supplementary Fig. 7b reveals that the parallelogram-shaped $ReSe_2$ flakes with parallel edges usually possess the same contrast and therefore have the same lattice orientation. Furthermore, BF-LEEM characterization of three merged $ReSe_2$ parallelograms was also carried out (Fig. 3c). Corresponding LEED patterns recorded from the three domains (denoted 4–6 in Fig. 3c) display three sets of patterns possessing different orientations (Fig. 3d), thereby indicating their different lattice orientations. Surprisingly, the orientations of the LEED patterns are firmly related to the directions of the short edges of each $ReSe_2$ parallelogram (see Fig. 3c, d), being positioned at approximately 11°, 142°, and 129° with regard to the horizontal direction. Further DF-LEEM image (Fig. 3e) exhibits clearly different contrasts among the three domains, and their merging boundaries are also clearly visible. Additional LEEM/LEED characterization of the orientation/boundary of the polygonal $ReSe_2$ domains is described in Supplementary Fig. 7c, d. It is worthy of mentioning that this domain orientation/boundary imaging method of LEEM/LEED is distinguished from the commonly used dark-field TEM method, which usually involves a sample transfer process[39–41]. DF-LEEM accompanied with μ-LEED techniques is thus promising for serving as an in situ, nondestructive, and high-throughput method for determining the crystal structure of anisotropic 2D monolayer $ReSe_2$ grown on conductive substrates. In addition, this identification method is also applicable to other 2D-layered materials synthesized on various conductive substrates.

Atomic and electronic structures of monolayer $ReSe_2$. The CVD-grown monolayer $ReSe_2$ on Au foil was also directly analyzed by high-resolution STM/STS to uncover its atomic-scale morphology and electronic properties in an as-grown state. Prior to the STM measurements, the CVD-grown $ReSe_2$/Au was degassed overnight at ~400 °C in an ultrahigh-vacuum chamber to remove adsorbed impurities. Figure 4a shows a large-scale STM image of the sample surface, in which a large-area monolayer $ReSe_2$ film is observed to extend over the flat Au terraces. The corresponding atomically resolved STM image (Fig. 4b) reveals perfect quasi-hexagonal surface lattices, indicating the relatively high crystal quality of the CVD-grown $ReSe_2$ flakes. The unit cell, which is composed of the brightest neighboring spots,

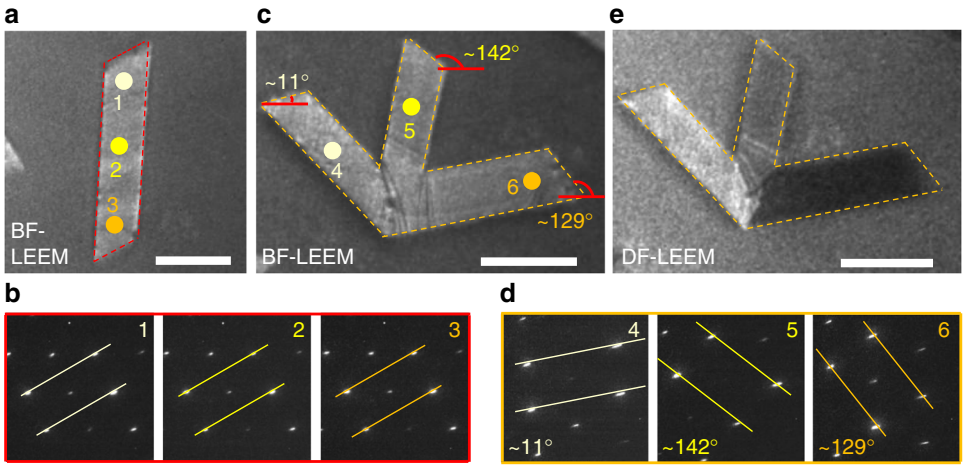

Fig. 3 In situ LEEM and μ-LEED characterization of the orientations and boundaries of monolayer $ReSe_2$ domains on Au foils. **a** LEEM image (at 7.3 eV) of a monolayer $ReSe_2$ parallelogram on Au foil. **b** LEED patterns (at 50 eV) from the regions marked 1–3 in **a** reconfirming the single-crystal nature of the sample. **c** BF-LEEM image (at 1.5 eV) of three merged $ReSe_2$ domains. **d** LEED patterns (at 50 eV) recorded from the domains denoted 4–6 in **c**. The angles of the marked solid lines with respect to the horizontal direction are labeled in the patterns. **e** DF-LEEM image (at 9.8 eV) from the same area in image (**c**) showing remarkably different contrasts for the three merged parallelograms. Scale bars, 5 μm in **a**, **c**, **e**

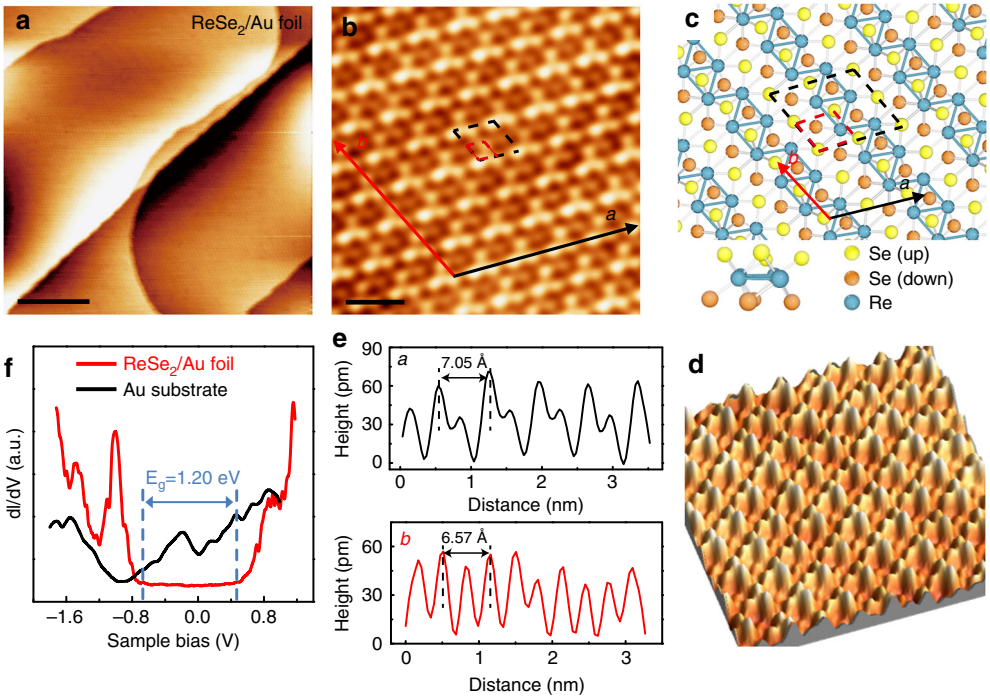

Fig. 4 Atomic structure and electronic properties of monolayer $ReSe_2$ on Au foils. **a** Large-scale STM image ($V_T = -0.05$ V, $I_T = 12.64$ nA; 215 nm × 215 nm) of as-grown monolayer $ReSe_2$ on a Au foil substrate. **b** Atomically resolved STM image (−0.003 V, 12.64 nA; 5.3 nm × 5.3 nm) revealing the perfect atomic lattice of CVD-grown $ReSe_2$. The unit cell and the top four non-identical Se atoms of $ReSe_2$ are marked by black and red dashed parallelograms, respectively. **c** Top and side views of the structural model of $ReSe_2$. The *a*-axis and *b*-axis, unit cell and top four Se atoms are denoted by black and red arrows, a black dashed parallelogram and a red dashed parallelogram, respectively. **d** Corresponding 3D STM image of the $ReSe_2$ lattice showing an undulating surface. **e** Height profiles along the two typical lattice orientations (*a*-axis and *b*-axis) revealing different lattice constants of ~7.05 and ~6.57 Å, respectively. **f** Typical STS spectra (1.50 V, 210 pA, $V_{rms} = 10$ mV, $f = 932$ Hz) taken on monolayer $ReSe_2$/Au (red) showing a band gap of ~1.20 eV and on the Au substrate (black) as a reference. Scale bars, 50 nm in **a** and 1 nm in **b**

and the four adjacent spots, which are characterized by gradually increasing STM contrasts, are indicated by the black and red dashed parallelograms, respectively. According to the atomic model in Fig. 4c, the observed spot-like contrasts (e.g., the four typical spots in the red dashed parallelogram) correspond to the upper Se atoms (e.g., four Se atoms) of $ReSe_2$. Additional sequential zoomed-in STM images are supplied in Supplementary Fig. 8 to show a $ReSe_2$ film covering terraced Au and the coexistence of atomic lattices and the underlying terraces.

Notably, the STM contrast variations inside each unit cell (indicated by the black dashed parallelogram) can be visually observed in the corresponding 3D STM image (Fig. 4d), which is

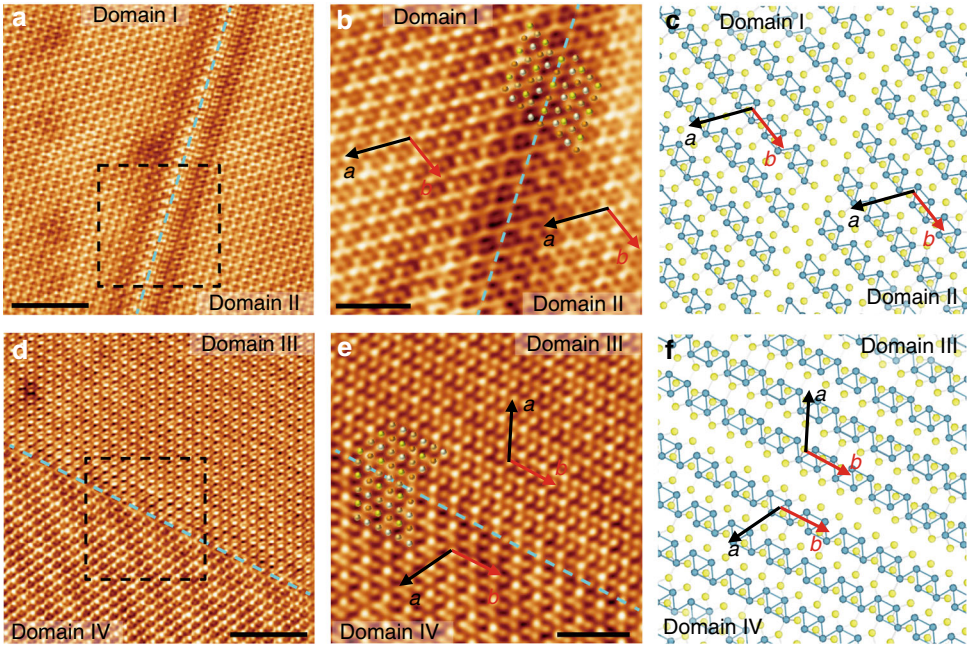

Fig. 5 STM images of two typical GBs in the $ReSe_2$/Au sample. **a** Large-scale STM image (−0.004 V, 12.64 nA; 20 nm × 20 nm) of a GB composed of a parallel dislocation between two adjacent $ReSe_2$ domains. **b** Magnified STM image (−0.003 V, 12.64 nA; 8.3 nm × 8.3 nm) of **a** with the fitted atomic models superimposed. The yellow dots with color gradients represent the upper Se atoms with different STM contrasts. The GB and the *a*-axis and *b*-axis of domains I and II are marked by a blue dashed line and black and red arrows, respectively. **c** Corresponding schematic illustration of the evolution of the GB shown in **a**, **b**. Only the upper layer Se atoms are shown here for clarity. The *a*-axis and *b*-axis of the two domains are marked by black and red arrows, respectively. **d** Large-scale STM image (−0.008 V, 30.77 nA; 20 nm × 20 nm) of a mirror twin GB. **e** Magnified STM image (−0.005 V, 30.77 nA; 8.30 nm × 8.30 nm) of **d** with the fitted atomic models superimposed. **f** Corresponding schematic illustration of the GB shown in **d**, **e**. Scale bars, 5 nm in **a**, **d** and 2 nm in **b**, **e**

in sharp contrast with the honeycomb-like lattices of MoS_2 possessing uniform spot-like contrasts inside each unit cell[28, 42]. This contrast fluctuation stems from the anisotropic structure of $ReSe_2$[12, 43]. Typically, $ReSe_2$ crystallizes in a distorted 1T structure, and the four typical Re atoms are arranged into a diamond-shaped chain along the *b*-axis direction (along the red arrow in Fig. 4c). This structural distortion breaks the hexagonal symmetry and affords a doubled unit cell size (indicated by the black dashed parallelogram) compared to the configuration of the initial four Se atoms (marked by the red dashed parallelogram). The four Se atoms are not all in the same plane[12, 43], which explains the varied contrasts in the STM image[44].

It has been reported that the two principal crystal axes of $ReSe_2$, corresponding to the shortest (*b*-axis) and second-shortest axis (*a*-axis) in the basal plane, have an angle of ~118.91° [22]. Herein, the height profiles taken along these two typical lattice directions (*a*-axis and *b*-axis; marked in Fig. 4b, plotted in Fig. 4e) reveal two lattice constants of 7.05 ± 0.2 and 6.57 ± 0.1 Å, respectively, in line with the previous report[45]. Furthermore, low-temperature (~78 K) STS measurements were also conducted to explore the electronic structure of monolayer $ReSe_2$/Au foils. As shown in Fig. 4f, the valence band maximum and conduction band minimum of $ReSe_2$/Au are located at ~−0.70 and +0.50 V, respectively, indicating a slight n-doping effect of monolayer $ReSe_2$ on Au foils. The quasiparticle band gap (E_g) of $ReSe_2$/Au (~1.20 eV) is evidently much smaller than the theoretical value (~2.09 eV)[43], probably due to the strong interfacial electronic interaction, which introduces metal-induced gap states to $ReSe_2$ from the Au substrate, as similarly reported for MoS_2 on Au foils with a reduced band gap[46, 47]. As a side evidence, the STS spectrum of the Au substrate shows an apparent tunneling contribution at a larger bias range than the band gap region of $ReSe_2$.

Detailed structures of $ReSe_2$ GBs. Current knowledge of the detailed structure of the GBs of structurally isotropic 2D materials, e.g., graphene and MoS_2, is relatively comprehensive, revealing the existence of 4-membered-ring, 5-membered-ring, 7-membered-ring or 8-membered-ring types of defects[39, 48–52]. However, for ReX_2, the large anisotropic interfacial energies imposed by their anisotropic structure make the structures of their GBs quite ambiguous, although efforts have been made using ex situ TEM characterization[26, 53]. In this work, detailed STM studies were first used to address such issues for the CVD-grown monolayer $ReSe_2$/Au system.

A typical GB with a bright line-shaped contrast (marked by a blue dashed line) was captured between two neighboring domains (Fig. 5a and Supplementary Fig. 9). Since the STM morphology of the two composite domains (marked I and II) are quite similar, identifying the *a*-axis and *b*-axis of each is essential to distinguish their domain orientations. This can be realized by mapping the height profiles along the three different lattice directions (Supplementary Fig. 9) considering the inequivalence of the $ReSe_2$ lattices[12, 43]. Consequently, domains I and II are revealed to have nearly the same lattice constants/orientations, and the *a*-axis and *b*-axis of the two domains are marked in Fig. 5b. Notably, in the further zoomed-in STM image in Fig. 5b, the bright line-shaped contrast at the GB almost disappears, and the patching interface becomes much clearer. The upper Se atoms imaged by STM are almost continuous at the GB but with a little distortion (as indicated by the fitted atomic model), which is free of apparent dislocation cores or defects. Accordingly, this patching behavior can be defined as two parallel domains with a dislocation, as also schematically shown in Fig. 5c for a clearer view.

Another typical GB is presented in Fig. 5d and Supplementary Fig. 10, wherein domains III and IV have apparently different

STM contrasts even in the large-scale STM image. A perfect lattice coherence between the two adjacent domains is noticeable in the magnified STM image in Fig. 5e (as indicated by the fitted atomic model). A similar method was also used to identify the orientation of each domain (Supplementary Fig. 10). The results indicate that for domains III and IV, the *b*-axis directions are the same, whereas the *a*-axes are reversed. In this regard, this typical GB can be considered as a mirror twin boundary, as schematically shown in Fig. 5f. To illustrate the atomic bonding feature at the two typical GBs mentioned above, density functional theory (DFT) calculations were also performed, and the results coincide well with the STM observations (Supplementary Fig. 11 and Supplementary Discussion). More STM images of the twist GBs are provided in Supplementary Fig. 12, and the patching interfaces are similarly free of obvious defects.

Previous STEM studies revealed that the GBs in ReX_2 evolved when the orientation of the Re-chain was changed by electron beam irradiation or the vacancy defects around the GBs[26, 53]. However, this ex situ characterization cannot avoid the artificial destruction induced by the transfer process and the effect of high-energy electron bombardment by TEM analysis. Accordingly, the intrinsic defect type of GBs may not be well resolved. In contrast, the CVD-grown $ReSe_2$/Au foil synthesized in this work serves as an ideal platform for uncovering the intrinsic structures of GBs using in situ STM/STS characterization. To the best of our knowledge, this is the first report of an STM study on the GBs of $ReSe_2$. Nevertheless, it is noteworthy that further theoretical and experimental efforts are still desirable for an in-depth understanding of the GBs.

Discussion

In summary, we have accomplished the highly uniform synthesis of high-quality monolayer $ReSe_2$ single crystals on Au foils using an APCVD method. We then identify the single-crystal nature of the parallelogram-shaped $ReSe_2$ domains by using various methods, including Raman spectroscopy, TEM, and LEEM/LEED. The novel monolayer growth of $ReSe_2$ on Au foils is directed by a self-limited catalytic growth mechanism, and the specific parallelogram shape is mainly mediated by its anisotropic structure. Direct growth on Au foil allows the atomic-scale morphology and intrinsic band feature of monolayer $ReSe_2$ directly on Au foils to be analyzed using in situ STM/STS. We believe that this work should pave the way towards the direct synthesis and in situ characterization of anisotropic 2D-layered materials such as $ReSe_2$ and propel their fundamental property investigations and practical applications in next-generation electronic and optoelectronic devices.

Methods

Synthesis of $ReSe_2$. The synthesis of single-crystalline monolayer $ReSe_2$ on Au foils was conducted in a multi-temperature-zone APCVD tube furnace equipped with a quartz tube (1 inch in diameter). Before growth, the Au foil (ZhongNuo Advanced Material Technology Co., Ltd., 30 μm thick, 99.99% purity) was annealed at 970 °C for 8 h to reduce its surface roughness. Five milligrams ReO_3 powder (Alfa Aesar, 99.9% purity) and 1 g Se powder (Alfa Aesar, 99 + % purity) were utilized as the Re and Se precursors for the CVD growth. The Au substrate with an area of 1 cm × 1 cm was placed in a quartz boat at the center of the furnace. To expel air, the tube furnace was first flushed with ultra-high-purity Ar gas. The furnace was then heated to 750 °C over 30 min and maintained at 750 °C for 15, 30, or 60 min for growth under a constant flow rate of Ar gas of 50 sccm and H_2 gas of 10 sccm at atmospheric pressure. After the synthetic procedure, the furnace was naturally cooled to room temperature.

Transfer of $ReSe_2$. For sample transfer, the $ReSe_2$/Au samples were first spin-coated with poly(methyl methacrylate) (PMMA) at 2500 rpm for 1 min, resulting in a uniform polymer film on the sample surfaces, and then were baked at 120 °C for 15 min. Next, the PMMA film, together with $ReSe_2$ flakes, was detached from the Au substrate using an electrochemical bubbling method[30]. PMMA-supported $ReSe_2$ was then washed with deionized water several times, transferred onto SiO_2(300 nm)/Si substrates or TEM grids, and dried on a hot plate at 80 °C. Finally, the PMMA was removed using acetone and isopropanol.

Characterization of $ReSe_2$. The synthesized $ReSe_2$ flakes were systematically characterized using SEM (Hitachi S-4800, 2 kV), AFM (Bruker Dimension Icon), Raman spectroscopy (HORIBA iHR550, excitation light wavelengths of 514 and 532 nm), XPS (Kratos Analytical AXIS-Ultra with monochromatic Al Kα X-ray), TEM (FEI Tecnai F20, acceleration voltage of 200 kV), STEM (JEOL JEM-ARM200CF, acceleration voltage of 200 kV), and LEEM/μ-LEED (Elmitec LEEM-III system with ultrahigh vacuum of ~1×10^{-10} Torr). Ultrahigh-vacuum low-temperature STM/STS systems were also utilized for the atomic-scale structural characterization under a base pressure of better than 10^{-10} mbar. All the STM images were obtained at room temperature. The STS spectra were acquired at ~78 K by recording the output of a lock-in system with the manually disabled feedback loop. A modulation signal of 10 mV at 932 Hz was selected under a tunneling condition of 1.50 V and 210 pA.

DFT calculations. DFT calculations were performed by the Vienna ab initio simulation package using the plane-wave basis set[54] with an energy cutoff of 450 eV and the projector-augmented wave[55] potentials and the generalized gradient approximation parameterized by Perdew, Burke and Ernzerhof for the exchange-correlation functional[56].

Data availability. The data reported by this article are available from the corresponding author upon reasonable request.

Received: 7 October 2017 Accepted: 22 January 2018
Published online: 22 March 2018

References

1. Novoselov, K. S. et al. Electric field effect in atomically thin carbon films. *Science* **306**, 666–669 (2004).
2. Geim, A. K. Graphene: status and prospects. *Science* **324**, 1530–1534 (2009).
3. Liao, L. et al. High speed graphene transistors with a self-aligned nanowire gate. *Nature* **467**, 305–308 (2010).
4. Radisavljevic, B. et al. Single-layer MoS_2 transistors. *Nat. Nanotechnol.* **6**, 147–150 (2011).
5. Wang, Q. H. et al. Electronics and optoelectronics of two-dimensional transition metal dichalcogenides. *Nat. Nanotechnol.* **7**, 699–712 (2012).
6. Voiry, D. et al. Enhanced catalytic activity in strained chemically exfoliated WS_2 nanosheets for hydrogen evolution. *Nat. Mater.* **12**, 850–855 (2013).
7. Chhowalla, M. et al. The chemistry of two-dimensional layered transition metal dichalcogenide nanosheets. *Nat. Chem.* **5**, 263–275 (2013).
8. Mak, K. F. et al. The valley Hall effect in MoS_2 transistors. *Science* **344**, 1489–1492 (2014).
9. Sie, E. et al. Valley-selective optical Stark effect in monolayer WS_2. *Nat. Mater.* **14**, 290–294 (2015).
10. Lu, A.-Y. et al. Janus monolayers of transition metal dichalcogenides. *Nat. Nanotechnol.* **12**, 744–749 (2017).
11. Tongay, S. et al. Monolayer behaviour in bulk ReS_2 due to electronic and vibrational decoupling. *Nat. Commun.* **5**, 3252 (2014).
12. Wolverson, D. et al. Raman spectra of monolayer, few-layer, and bulk $ReSe_2$: an anisotropic layered semiconductor. *ACS Nano* **8**, 11154–11164 (2014).
13. Hart, L. et al. Rhenium dichalcogenides: layered semiconductors with two vertical orientations. *Nano Lett.* **16**, 1381–1386 (2016).
14. Zhang, Q. et al. Edge-to-edge oriented self-assembly of ReS_2 nanoflakes. *J. Am. Chem. Soc.* **138**, 11101–11104 (2016).
15. Zhang, Q. et al. Extremely weak van der Waals coupling in vertical ReS_2 nanowalls for high-current-density lithium-ion batteries. *Adv. Mater.* **28**, 2616–2623 (2016).
16. Liu, E. et al. Integrated digital inverters based on two-dimensional anisotropic ReS_2 field-effect transistors. *Nat. Commun.* **6**, 6991 (2015).
17. Chenet, D. A. et al. In-plane anisotropy in mono- and few-layer ReS_2 probed by Raman spectroscopy and scanning transmission electron microscopy. *Nano Lett.* **15**, 5667–5672 (2015).
18. Yang, S. et al. Tuning the optical, magnetic, and electrical properties of $ReSe_2$ by nanoscale strain engineering. *Nano Lett.* **15**, 1660–1666 (2015).
19. Lorchat, E. et al. Splitting of interlayer shear modes and photon energy dependent anisotropic raman response in n-layer $ReSe_2$ and ReS_2. *ACS Nano* **10**, 2752–2760 (2016).
20. Arora, A. et al. Highly anisotropic in-plane excitons in atomically thin and bulklike 1T'-$ReSe_2$. *Nano Lett.* **17**, 3202–3207 (2017).
21. Liu, F. et al. Highly sensitive detection of polarized light using anisotropic 2D ReS_2. *Adv. Funct. Mater.* **26**, 1169–1177 (2016).
22. Zhang, E. et al. Tunable ambipolar polarization-sensitive photodetectors based on high-anisotropy $ReSe_2$ nanosheets. *ACS Nano* **10**, 8067–8077 (2016).

23. Yang, H. et al. Optical waveplates based on birefringence of anisotropic two dimensional layered materials. *ACS Photonics* **4**, 3023–3030 (2017).
24. Hafeez, M. et al. Chemical vapor deposition synthesis of ultrathin hexagonal $ReSe_2$ flakes for anisotropic Raman property and optoelectronic application. *Adv. Mater.* **28**, 8296–8301 (2016).
25. Jiang, S. et al. Application of chemical vapor–deposited monolayer $ReSe_2$ in the electrocatalytic hydrogen evolution reaction. *Nano Res.* https://doi.org/10.1007/s12274-017-1796-8 (2017).
26. Lin, Y.-C. et al. Single-layer ReS_2: two-dimensional semiconductor with tunable in-plane anisotropy. *ACS Nano* **9**, 11249–11257 (2015).
27. Shi, J. et al. Monolayer MoS_2 growth on Au foils and on-site domain boundary imaging. *Adv. Funct. Mater.* **25**, 842–849 (2015).
28. Zhou, X. et al. Periodic modulation of the doping level in striped MoS_2 superstructures. *ACS Nano* **10**, 3461–3468 (2016).
29. Shi, J. et al. Substrate facet effect on the growth of monolayer MoS_2 on Au foils. *ACS Nano* **9**, 4017–4025 (2015).
30. Gao, Y. et al. Large-area synthesis of high-quality and uniform monolayer WS_2 on reusable Au foils. *Nat. Commun.* **6**, 8569 (2015).
31. Yun, S. J. et al. Synthesis of centimeter-scale monolayer tungsten disulfide film on gold foils. *ACS Nano* **9**, 5510–5519 (2015).
32. Gao, Y. et al. Ultrafast growth of high-quality monolayer WSe_2 on Au. *Adv. Mater.* **29**, 1700990 (2017).
33. Knook, B. et al. The electrical resistance of some dilute alloys of the noble metals and Re at low temperatures. *Physica* **30**, 1124–1130 (1964).
34. Li, X. et al. Large-area synthesis of high-quality and uniform graphene films on copper foils. *Science* **324**, 1312–1314 (2009).
35. Shi, J. et al. Controllable growth and transfer of monolayer MoS_2 on Au foils and its potential application in hydrogen evolution reaction. *ACS Nano* **8**, 10196–10204 (2014).
36. Gao, L. et al. Repeated growth and bubbling transfer of graphene with millimeter-size single-crystal grains using platinum. *Nat. Commun.* **3**, 699 (2012).
37. Mu, R. et al. Visualizing chemical reactions confined under graphene. *Angew. Chem. Int. Ed.* **51**, 4856–4859 (2012).
38. Ning, Y. et al. Applications of PEEM/LEEM in dynamic studies of surface physics and chemistry of two-dimensional atomic crystals. *Acta Phys. Chim. Sin.* **32**, 171–182 (2016).
39. Van der Zande, A. M. et al. Grains and grain boundaries in highly crystalline monolayer molybdenum disulphide. *Nat. Mater.* **12**, 554–561 (2013).
40. Najmaei, S. et al. Vapour phase growth and grain boundary structure of molybdenum disulphide atomic layers. *Nat. Mater.* **12**, 754–759 (2013).
41. Ji, Q. et al. Unravelling orientation distribution and merging behavior of monolayer MoS_2 domains on sapphire. *Nano Lett.* **15**, 198–205 (2015).
42. Huang, Y. L. et al. Bandgap tunability at single-layer molybdenum disulphide grain boundaries. *Nat. Commun.* **6**, 6298 (2015).
43. Zhong, H. X. et al. Quasiparticle band gaps, excitonic effects, and anisotropic optical properties of the monolayer distorted 1T diamond-chain structures ReS_2 and $ReSe_2$. *Phys. Rev. B* **92**, 115438 (2015).
44. Parkinson, B. A. et al. Relationship of STM and AFM images to the local density of states in the valence and conduction bands of rhenium selenide ($ReSe_2$). *J. Am. Chem. Soc.* **113**, 7833–7837 (1991).
45. Lamfers, H.-J. et al. The crystal structure of some rhenium and technetium dichalcogenides. *J. Alloys Compd.* **241**, 34–39 (1996).
46. Lee, S. et al. Statistical study on the schottky barrier reduction of tunneling contacts to CVD synthesized MoS_2. *Nano Lett.* **16**, 276–281 (2016).
47. Zhang, Z. et al. Direct chemical vapor deposition growth and band-gap characterization of MoS_2/h-BN van der Waals heterostructures on Au foils. *ACS nano* **11**, 4328–4336 (2017).
48. Yang, B. et al. Periodic grain boundaries formed by thermal reconstruction of polycrystalline graphene film. *J. Am. Chem. Soc.* **136**, 12041–12046 (2014).
49. Zhang, Z. et al. Unraveling the sinuous grain boundaries in graphene. *Adv. Funct. Mater.* **25**, 367–373 (2015).
50. Zhou, W. et al. Intrinsic structural defects in monolayer molybdenum disulfide. *Nano Lett.* **13**, 2615–2622 (2013).
51. Zou, X. et al. Predicting dislocations and grain boundaries in two-dimensional metal-disulfides from the first principles. *Nano Lett.* **13**, 253–258 (2013).
52. Huang, Y. L. et al. Gap states at low-angle grain boundaries in monolayer tungsten diselenide. *Nano Lett.* **16**, 3682–3688 (2016).
53. Wu, K. et al. Domain architectures and grain boundaries in chemical vapor deposited highly anisotropic ReS_2 monolayer films. *Nano Lett.* **16**, 5888–5894 (2016).
54. Kresse, G. et al. Efficient iterative schemes for ab initio total-energy calculations using a plane-wave basis set. *Phys. Rev. B* **54**, 11169–11186 (1996).
55. Kresse, G. et al. From ultrasoft pseudopotentials to the projector augmented-wave method. *Phys. Rev. B* **59**, 1758–1775 (1999).
56. Perdew, J. P. et al. Generalized gradient approximation made simple. *Phys. Rev. Lett.* **77**, 3865–3868 (1996).

Acknowledgements

The work was supported by the National Natural Science Foundation of China (Nos. 51290272, 51472008, 21688102, 61774003, and 21573004), the National Key Research and Development Program of China (2016YFA0200103, 2016YFA0200200, 2017YFA0304600, and 2017YFA0205700), and the Open Research Fund Program of the State Key Laboratory of Low-Dimensional Quantum Physics (Nos. KF201601 and KF201604).

Author contributions

Y.Z. conceived and supervised the research project. S.J. performed CVD growth and transfer of $ReSe_2$, with Z. Z., P.Y., X. Z., C. X., J.S., and Y.H.'s assistance. M.H. carried out the STM/STS characterization. W.W., and Q.F. performed the LEEM/LEED characterization. S.J., Z.Z., P.Y., X.Z., C.X., J.S., and Y.H. carried out the optical microscopy, XPS, SEM, AFM, TEM, and STEM characterizations. L.Z., N.Z., L.T., and Q.Z. performed Raman spectroscopy characterization. N.G. and J.Z. performed the DFT calculations. S.J., M.H., Q.F., and Y.Z. co-wrote the manuscript and all authors contributed to the critical discussions of the manuscript.

Additional information

Supplementary information accompanies this paper at https://doi.org/10.1038/s42004-018-0010-6.

Competing interests: The authors declare no competing interests.

Reprints and permission information is available online at http://npg.nature.com/reprintsandpermissions/

Publisher's note: Springer Nature remains neutral with regard to jurisdictional claims in published maps and institutional affiliations.